Friction between a plane strain circular indenter and a thick poroelastic substrate

Yuan Qi[1], Kristin N. Calahan[1], Mark E. Rentschler[1], Rong Long[1*]

[1]Department of Mechanical Engineering, University of Colorado Boulder, Boulder, CO, 80309, USA

*Corresponding author: rong.long@colorado.edu

Abstract

This paper presents a computational study on the role of poroelasticity in gel friction. Motivated by recent experimental studies in the literature, we develop a plane strain finite element model to elucidate the contact mechanics between a circular indenter and a thick poroelastic substrate under both normal and shear loadings. Two cases are considered: i) steady state sliding under fixed normal displacements, and ii) relaxation under fixed normal and shear displacements. In steady state sliding, we find that a net friction force can arise even if no intrinsic adhesive or frictional interaction is implemented at the indenter/substrate interface. Such friction force exhibits a non-monotonic dependence on the sliding velocity and peaks at an intermediate velocity. Our model reveals that this friction force is induced by poroelastic diffusion in the gel substrate which can lead to considerable asymmetry in both the contact profile and contact pressure. In terms of relaxation, if the indenter/substrate interface is set to be frictionless, we find that the friction force induced by poroelasticity relaxes to zero with a characteristic time much faster than that of the normal force. When a finite friction coefficient is introduced at the interface, the normalized relaxation curve for the friction force approaches that for the normal force as the friction coefficient increases. These modeling results suggest that poroelasticity can be an important contributing mechanism for gel friction.

Keywords: Friction, poroelasticity, finite element simulations, steady state sliding, relaxation.

1. Introduction

The friction of gels is a fundamental problem ubiquitously found in biological systems (e.g., cartilage) and engineering applications (e.g., contact lens). For example, the friction of biological interfaces involving cartilage (Ateshian, 2009; Krishnan et al., 2004; Moore and Burris, 2014) and mucous surfaces (Pult et al., 2015) is directly related to the lubrication and wear of tissues, and thus is of critical importance for applications including artificial joints (Greene et al., 2011, 2008; Jin et al., 1992; McCutchen, 1962) and regenerative medicine (Sterner et al., 2017). More recently, the need to develop medical robotic devices with *in vivo* mobility (Sliker et al., 2012) demands a fundamental understanding of the friction between synthetic materials and biological tissues (Sliker et al., 2010). Unlike macroscopic stiff surfaces that follow Amontons' laws of friction, many biological interfaces are soft, aqueous and dynamic (Gong, 2006; Pitenis et al., 2017), thereby exhibiting complex frictional behaviors far beyond Amontons' laws (Gong et al., 1997). In this regard, hydrogels provide an ideal model system to enable experimental and theoretical investigations on the friction of soft and aqueous interfaces (Gong, 2006). Extensive experimental studies in the literature have revealed that gel friction depends on a wide range of parameters which can be largely categorized into three types: i) loading parameters such as sliding velocity (Delavoipière et al., 2018; Gong et al., 1997; Reale and Dunn, 2017) and normal pressure (Gong et al., 1997), ii) surface conditions such as roughness (Persson and Scaraggi, 2018; Yashima et al., 2014) and interface fluid domain (Yamamoto et al., 2014), and iii) gel properties such as network mesh size (Shoaib et al., 2018), electric charges (Gong et al., 2002), and water content (Dunn et al., 2013).

The dependence on the sliding velocity, referred to as the rate-dependence hereafter, is a key feature of gel friction. Several physical mechanisms can contribute to the rate-dependence of gel friction. The theory established by Gong and Osada (1998) described the interplay of two mechanisms: adhesion and hydrodynamic lubrication. Specifically, this model considers two cases of surface interaction between a hydrogel and a substrate when immersed in water: repulsive or attractive. For the repulsive case, friction is governed by the lubrication of the hydrated water layer of the gel network at the interface. For the attractive case, the adsorption and detachment of gel polymer chains on the substrate surface results in rate-dependent interface adhesion, and thus can also contribute to friction in addition to the lubrication layer. Such adhesive friction was modeled by tracking the stretch of adsorbed chains and the kinetics of chain adsorption and detachment,

similar to Schallamach's theory of rubber friction (Schallamach, 1963). As the sliding velocity increases, the dominant mechanism transitions from adhesive interaction to hydrodynamic lubrication (Kurokawa et al., 2005). For either adhesion or lubrication, the mechanism described above only accounts for what occurs at the interface. Most gels exhibit rate-dependent, inelastic bulk properties, e.g., viscoelasticity and poroelasticity, which can also lead to rate-dependent friction by inducing energy dissipation upon contact deformation (Delavoipière et al., 2018; Kagata et al., 2002; Rennie et al., 2005; Shoaib and Espinosa-Marzal, 2018). Several recent works were devoted to the coupling between bulk dissipative behavior and interface adhesion (Shoaib and Espinosa-Marzal, 2018) or hydrodynamic lubrication (Smyth and Green, 2017), and how such coupling governs gel friction.

This work focuses on a particular aspect of gel friction: the role of poroelasticity. In recent experimental studies on gel friction, it was found that poroelastic diffusion in the gel substrate can lead to an asymmetric contact area (Delavoipière et al., 2018) and rate-dependent kinetic friction (Delavoipière et al., 2018; Reale and Dunn, 2017). Prior to these works, the poroelastic relaxation in gel substrates upon normal contact with a cylindrical indenter (Hui et al., 2006) or a spherical indenter (Hu et al., 2011, 2010) was leveraged as a method to characterize the elasticity and permeability of gels. Theoretical or computational analyses of the poroelastic contact mechanics involving lateral displacements of the indenter are important for understanding the effect of poroelasticity on gel friction. Delavoipière et al. (2018) developed an analytical model to quantify how poroelasticity affects the contact pressure between a rigid spherical indenter and a thin gel layer under steady state sliding. However, in comparison to normal contact, the analyses of poroelastic contact mechanics with lateral displacements are still limited. Here we present a two-dimensional (2D) finite element analysis on the poroelastic contact mechanics between a rigid circular indenter and a thick gel substrate under the plane strain condition. In Section 2, we highlight relevant experimental results in the literature and define two problems for our finite element model: steady state sliding under fixed normal displacements and relaxation under fixed normal and shear displacements. Modeling results for these two problems are presented and discussed in Sections 3 and 4, respectively, and conclusions are provided in Section 5.

2. Problem definition

2.1 Experimental results in the literature

In this section, we briefly review relevant experimental works in the literature (Delavoipière et al., 2018; Johannes et al., 2019; Reale and Dunn, 2017) to put our work into perspective. These studies adopted similar experimental configurations, i.e., shearing a rigid spherical probe indented on a gel substrate as shown in Fig.1a. Two types of loading conditions are discussed here: steady state sliding and relaxation.

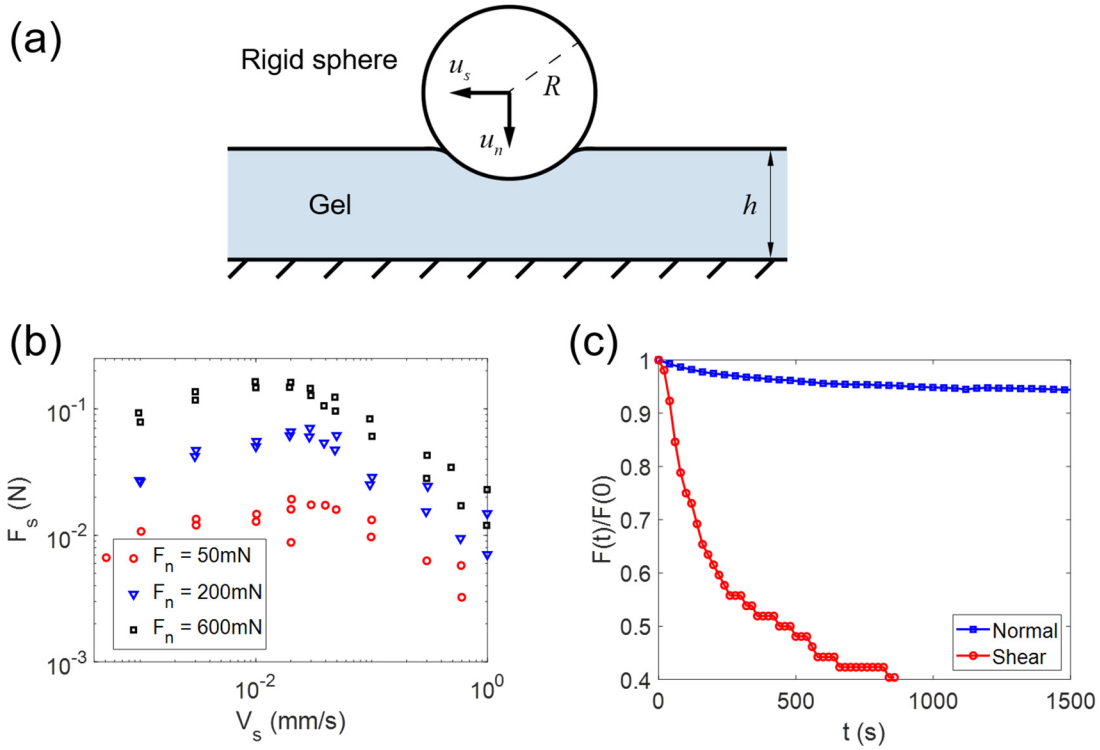

Figure 1 (a) Schematic showing the experimental configuration of a rigid sphere indenting and shearing on a gel substrate. (b) Experimental data from literature showing kinetic friction force F_s under steady state sliding with fixed normal forces F_n versus sliding velocity V_s. Data points are extracted from Figure 2 of Delavoipière et al. (2018). (c) Experimental data from literature showing the relaxation of normal or shear force under fixed normal or shear displacements. Data points for the normal force are extracted from the last step loading in Figure 3C (normal) of Johannes et al. (2019) and then normalized. Data points for the shear force are extracted from the first step loading in Figure 4A (shear) of Johannes et al. (2019) and then normalized.

Regarding steady state sliding, Delavoipière et al. (2018) used a glass sphere (R = 25.9mm) on a thin poly(dimethylacrylamide) gel layer (h =3.1μm) bonded to a glass surface, while Reale and Dunn (2017) used a smaller glass sphere (R =1.7mm) on a thick polyacrylamide gel substrate (h =

9mm). Despite the differences in dimension and material, both works showed that the kinetic friction force F_s under steady state sliding with a fixed normal force depends on the sliding velocity V_s (see Fig.1b). This rate dependence was attributed to the competition between poroelastic diffusion in the bulk gel and the advection caused by indenter sliding, which was characterized by the Péclet number *Pe*. It is important to note that the definitions of Péclet number in Delavoipière et al. (2018) and Reale and Dunn (2017) differ by a factor of order 1 but are consistent in terms of scaling analysis (see Appendix 1 for a detailed discussion). The experimental results in Delavoipière et al. (2018) show that the kinetic friction force F_s is a non-monotonic function of the sliding velocity V_s as illustrated in Fig.1b. The range of sliding velocity corresponds to $0.04 <\sim Pe <\sim 400$, and the friction force peaks at $Pe \sim 1$. On the other hand, Reale and Dunn (2017) showed that the friction coefficient (or friction force under a fixed normal force) decreases with *Pe*, but their experiments cover the range of $3.5 \leq Pe \leq 5500$ which presumably falls onto the decaying branch of friction coefficient versus *Pe*.

Two different approaches were developed to model the dependence of kinetic friction on *Pe*: Delavoipière et al. (2018) considered the energy dissipation due to poroelastic diffusion, whereas Reale and Dunn (2017) factored the effect of poroelastic relaxation into an effective, rate-dependent adhesion energy. In principle, these two approaches may be reconciled by recognizing that energy dissipation can lead to an increase in the effective adhesion energy as in the adhesion of viscoelastic solids (Barthel and Frétigny, 2009). Nevertheless, both approaches are based on energetics. Delavoipière et al. (2018) also developed an analytical model to address the underlying mechanics for the steady state sliding of a rigid spherical indenter on a thin gel substrate. Because of the thin substrate, they first used the elastic foundation approximation to determine the normal strain in the substrate. Using this approximate strain solution, they further calculated the pore pressure field and the interface contact pressure. The model showed that the contact area was circular for $Pe < 1$, but became asymmetric when $Pe > 1$. Interestingly, in both regimes the contact pressure was found to be asymmetric, i.e., the contact pressure near the leading edge of the indenter was larger than that near the trailing edge, which was induced by the uneven pore pressure in the gel substrate. This result implies that even if the interface is intrinsically frictionless, the poroelasticity could still induce a net friction force through the asymmetric contact pressure. However, since the model by Delavoipière et al. (2018) was approximate and only applicable in the thin substrate limit, whether this implication holds for other geometry (e.g., thick substrate) is

unclear. If it holds, what governs the rate-dependence of poroelasticity induced friction? These questions will be addressed in Section 3.

The previous works reviewed above focus on the rate-dependent kinetic friction force under fixed normal forces. In a recent work (Johannes et al., 2019), we studied the three-dimensional (3D) contact area of a spherical indenter (steel core coated by an elastomer layer with total radius R =265μm) on a polyacrylamide gel substrate (h =420μm). Significant relaxation of normal or shear force was observed under step loadings of normal or shear displacement. For example, the time history of normal and shear forces, normalized by their values at the beginning of relaxation, is shown in Fig.1c. Note that the time in Fig.1c is defined relative to the beginning of relaxation, i.e., just after a step loading of normal or shear displacement is applied. These results show that the shear force relaxes faster and to a much larger extent than the normal force. Although poroelastic relaxation in hydrogel substrates under normal indentation has been extensively modeled (Hu et al., 2011, 2010; Hui et al., 2006), studies on the relaxation under shear displacements are lacking, which will be explored in Section 4.

2.2 Finite element model

We build a finite element (FE) model using the commercial software ABAQUS (version 2017, Simulia, Dassault Systèmes, Providence, RI) to study the effect of poroelasticity on gel friction. Since gel friction involves multiple contributing mechanisms, we make the following assumptions to capture the key effects of poroelasticity while keeping the model tractable.

- ***Plane strain condition***: the 3D deformation induced by shear loadings of a spherical indenter on a gel substrate is computationally expensive to simulate. Therefore, here we consider a 2D plane strain model consisting of a rigid circular indenter (radius = R) on a gel substrate (thickness = h).
- ***Thick substrate*** (h>>R): we assume the limit of thick gel substrate (i.e., h >> R) to reduce the number of independent parameters, although in experiments the ratio h/R can cover a large range, e.g., ~10^{-4} in Delavoipière et al. (2018) and 5 in Reale and Dunn (2017).
- ***Linear poroelasticity model***: we assume the gel substrate undergoes infinitesimal displacement and strain during indentation and shear, which allows us to use the linear poroelastic model

(Cheng, 2016) and adopt the linear kinematics by turning off the "NLGEOM" option in ABAQUS.

- ***No adhesion at the interface***: interfacial adhesion can be a potentially significant contributing mechanism for gel friction (Gong and Osada, 1998). Here we assume zero adhesion at the interface between the indenter and the gel substrate to isolate the effect of poroelasticity.
- ***Friction on the interface***: we first assume the interface to be frictionless and check whether a net friction force can arise solely due to poroelastic diffusion. Next, the model will be extended to include a finite friction coefficient μ at the interface.

In reality, a fluid layer may be present between the indenter and the gel substrate, which can influence the friction and adhesion on the interface. For example, the fluid layer can reduce friction through hydrodynamic lubrication. As described in Section 1, this effect has been considered in the gel friction theory by Gong and Osada (1998). As for adhesion, usually it is weak, if not zero, when the contact interface is submerged in fluids (Delavoipière et al., 2018; Johannes et al., 2019; Reale and Dunn, 2017). In certain cases, an interfacial fluid layer may enhance adhesion through capillary interaction (Bhushan, 2003). In this work, we assume zero adhesion and adopt simple interface friction models (i.e., frictionless or constant friction coefficient) in order to focus on the effect of poroelasticity.

The linear poroelastic solid model implemented in our FE simulations is briefly described as follows. We treat the gel substrate as an isotropic, fully saturated poroelastic medium, and assume both the solid and fluid constituents are incompressible. In this case, the stress-strain relation is given by (Cheng, 2016):

$$\sigma_{mn} = 2G\varepsilon_{mn} + \frac{2G\nu}{1-2\nu}\varepsilon_{ss}\delta_{mn} - p\delta_{mn}, \tag{1}$$

where σ_{mn} is the stress component, ε_{mn} is the strain component, G is the shear modulus, ν is the Poisson's ratio in the fully drained state, p is the pore pressure, and δ_{mn} is the Kronecker delta. Note that the subscripts (e.g., m, n or s) ranges from 1 to 3 and the Einstein's summation convention of summing over repeated indices is adopted. The flux vector $\mathbf{q}$, i.e., the volume of fluid passing through a unit area per unit time, is governed by the Darcy's law:

$$\mathbf{q} = -\frac{k}{\eta}\nabla p, \tag{2}$$

where k is the intrinsic permeability (unit: m^2) and η is the dynamic viscosity of the fluid constituent (unit: Pa.s). Since both the solid and fluid constituents are incompressible, the bulk strain ε_{ss} can only be due to fluid transport, which leads to the following continuity equation:

$$\frac{\partial \varepsilon_{ss}}{\partial t} + \nabla \bullet \mathbf{q} = 0 \ , \tag{3}$$

where t is the time. Combining the strain compatibility equations and eq.(1), we can obtain the following harmonic equation (Cheng, 2016):

$$\nabla^2 \left(p - \frac{2(1-\nu)G}{(1-2\nu)} \varepsilon_{ss} \right) = 0 . \tag{4}$$

Substituting eq.(2) and eq.(4) into eq.(3), we obtain a diffusion equation in terms of the bulk strain ε_{ss}:

$$\frac{\partial \varepsilon_{ss}}{\partial t} - D\nabla^2 \varepsilon_{ss} = 0 , \tag{5}$$

where the diffusivity D is defined as

$$D = \frac{k}{\eta} \frac{2(1-\nu)G}{(1-2\nu)} . \tag{6}$$

To facilitate the FE similations, we set the shear modulus G = 27.9 kPa and drained Poisson's ratio ν = 0.28 according to Hu et al. (2010). Without loss of generality, the permeability is set to be k = 9.9×10^{-9} m^2. Note that the permeability k^* in ABAQUS (unit: m/s) has a different definition from k in eq.(2). They are related by

$$k^* = \frac{\gamma_w}{\eta} k , \tag{7}$$

where γ_w is the specific weight (i.e., weight per unit volume) of the fluid constituent. We use default values for both γ_w and η which correspond to γ_w =10^3 N/m^3 and η = 10^3 Pa.s. As a result, the diffusivity is D = 9.04×10^{-7} m^2/s.

The geometry, boundary conditions and loading history of our FE model are illustrated in Fig.2. Figure 2a shows the 2D plane strain mesh. The thickness h and width w of the gel substrate are far larger than the radius (R=30mm) of the rigid circular indenter, *i.e.*, h = 50R and w = 100R. The

bottom boundary is fixed and impermeable, while the other three boundaries are free and subjected to zero pore pressure. The contact between the rigid indenter and the gel substrate is assumed to be hard contact. In addition, the contacting interface is assumed to be frictionless or frictional with a coefficient μ. The gel substrate is meshed by 73766 CPE4P four-point quadrilateral elements with the smallest element size $l_{\min} = R/120$ within the contact region such that there are at least 55 elements at the contact interface (see Fig.2a). The "Soil" analysis step in ABAQUS Standard is applied to simulate the poroelastic response of the gel substrate. Additional details on the effect of damping factor and substrate width w are given in Appendix 2. Although friction experiments (Delavoipière et al., 2018; Reale and Dunn, 2017) are typically conducted under fixed normal forces, here we apply displacement boundary conditions in both the normal and shear directions to ensure convergence of the simulations. Specifically, two cases of loading histories are considered as shown in Fig.2b and Fig.2c. In both cases, a normal indentation displacement u_n is first applied with a velocity of 10mm/s and then held fixed for the rest of the simulation. The first case corresponds to steady state sliding, where the shear displacement u_s is continuously increased at a fixed velocity V_s (see Fig.2b). The second case is for shear force relaxation, where u_s is first increased at a fixed rate and then held fixed. The directions of u_n and u_s are shown in Fig.1a. The normal indentation depth in all simulations is kept small (u_n = 1 mm, 2 mm or 3 mm) to satisfy the infinitesimal deformation assumption.

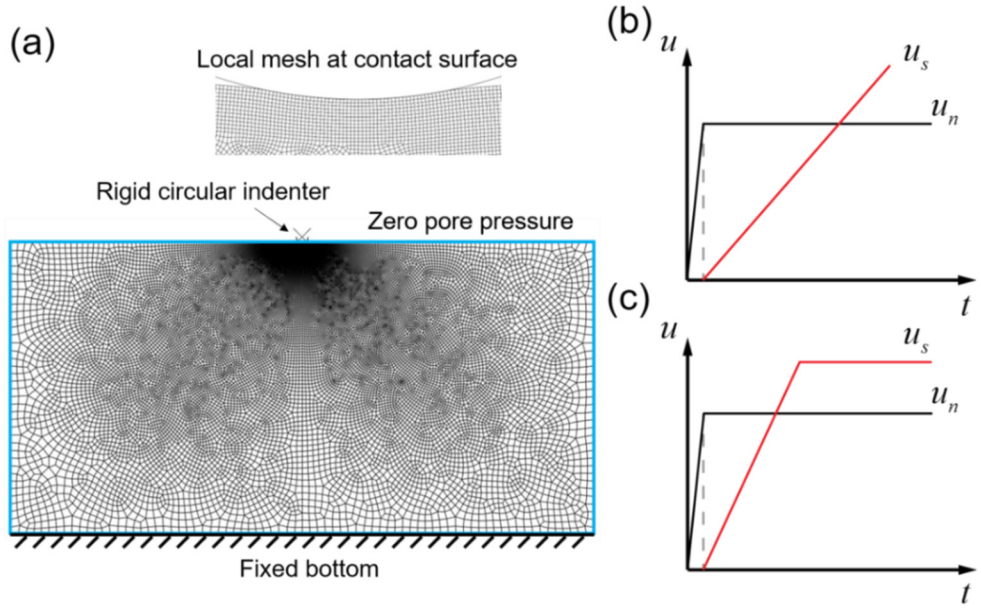

Figure 2 (a) Mesh geometry and boundary condition of the FE model. (b) Loading history of the normal displacement u_n and shear displacement u_s for steady state sliding. (c) Loading history of u_n and u_s for shear force relaxation.

3. Steady state sliding

3.1 Frictionless interface

We first focus on the case of steady state sliding with a frictionless interface. Under continuous sliding with a fixed normal displacement (see Fig.2b), we find that the indenter experiences a net friction force (see Fig.3b) even though the interface is frictionless with zero shear traction. Figure 3b also shows that the net friction force reaches a steady state value after a transient stage, and the steady state friction exhibits a non-monotonic dependence on the sliding velocity V_s. In Fig.3a, we plot the steady state friction F_s as a function of V_s for three normal indentation depths u_n (= 1, 2, or 3 mm). These results show that F_s increases with the indentation depth u_n at a fixed V_s, but the velocity V_{smax} at which the peak friction occurs slightly decreases with u_n (see Fig.3c).

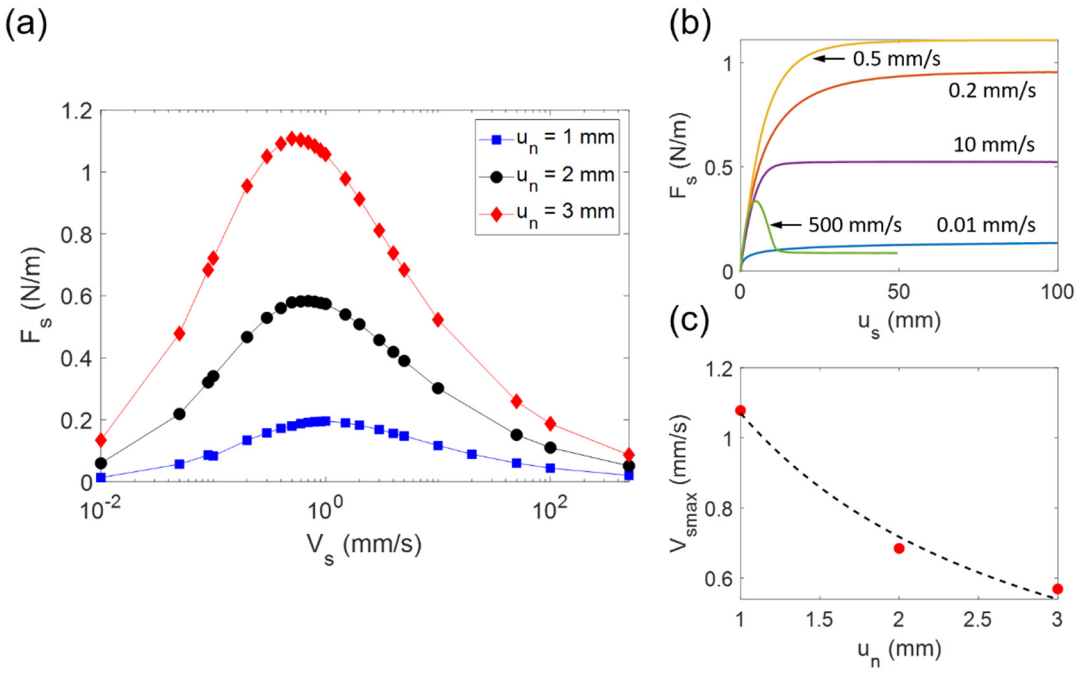

Figure 3 (a) Steady state friction force F_s versus the sliding velocity V_s for three different normal displacements (u_n = 1, 2, and 3 mm). (b) The friction force F_s versus shear displacement u_s at given sliding velocities (normal displacement u_n =3 mm). (c) The sliding velocity V_{smax} where peak friction force occurs decays slightly with the prescribed normal displacement u_n. The symbols are extracted from part (a) and the dashed line is given by an empirical fitting formula, V_{smax} =2.18/(u_n+1.03) to guide the view.

To understand the underlying mechanics of the steady state friction response, we show in Fig.4 the FE results for a representative case with u_n= 3 mm and V_s = 0.7 mm/s. For comparison, the same loading condition is applied to a control case where the substrate is elastic with the same G and ν(= 0.28) as the drained pororelastic solid. Results from the elastic control case are also shown in Fig.4. Since the interface is frictionless, the net friction force, if any, should come from the normal pressure p_c within the contact region. In Fig.4a where the arc angle θ is used to describe the location within the contact region, we see that the contact pressure p_c is asymmetric about the center of the indenter: p_c along the leading edge of the contact region (i.e., on the left of the indenter center) is considerably higher than the trailing edge. This is associated with an asymmetric contact region: the leading edge is wider than the trailing edge. As a result, integral of the horizontal component of p_c in the contact region leads to a non-zero net force resisting the sliding motion, i.e., the friction force. In contrast, Fig.4b shows that for the elastic control, the contact region and p_c are symmetric about the center of the indenter, which implies a zero net friction force. The zero net friction force for the elastic control is expected since sliding does not induce any additional deformation due to the frictionless interface, and the distribution of p_c should be the same as that for pure normal indentation. To illustrate this point, we note that analytical solution for p_c under normal indentation is available based on the plane strain Hertz solution (Johnson, 1987):

$$p_c = \frac{2F_n}{\pi a}\left(1-\frac{x^2}{a^2}\right)^{1/2}, \tag{8}$$

where F_n is the normal compressive force, x is the horizontal coordinate measured from the center of contact region, and a is the half contact width. The contact width a is related to the normal force by:

$$a^2 = \frac{2(1-\nu)F_n R}{\pi G}, \tag{9}$$

where R is the indenter radius. Since $x = R\sin\theta$, eq.(8) can be rewritten as

$$\frac{p_c}{G} = \frac{1}{(1-\nu)}\left(\frac{a^2}{R^2}-\sin^2\theta\right)^{1/2}, \text{ where } |\theta| \le \sin^{-1}\left(\frac{a}{R}\right). \tag{10}$$

Using the value of F_n from the FE result, we first calculate a using eq.(9) and then plot eq.(10) in Figs.4a and 4b as the dashed line. It can be seen that eq.(10) agrees well with the FE result of elastic control, but not the poroelastic case.

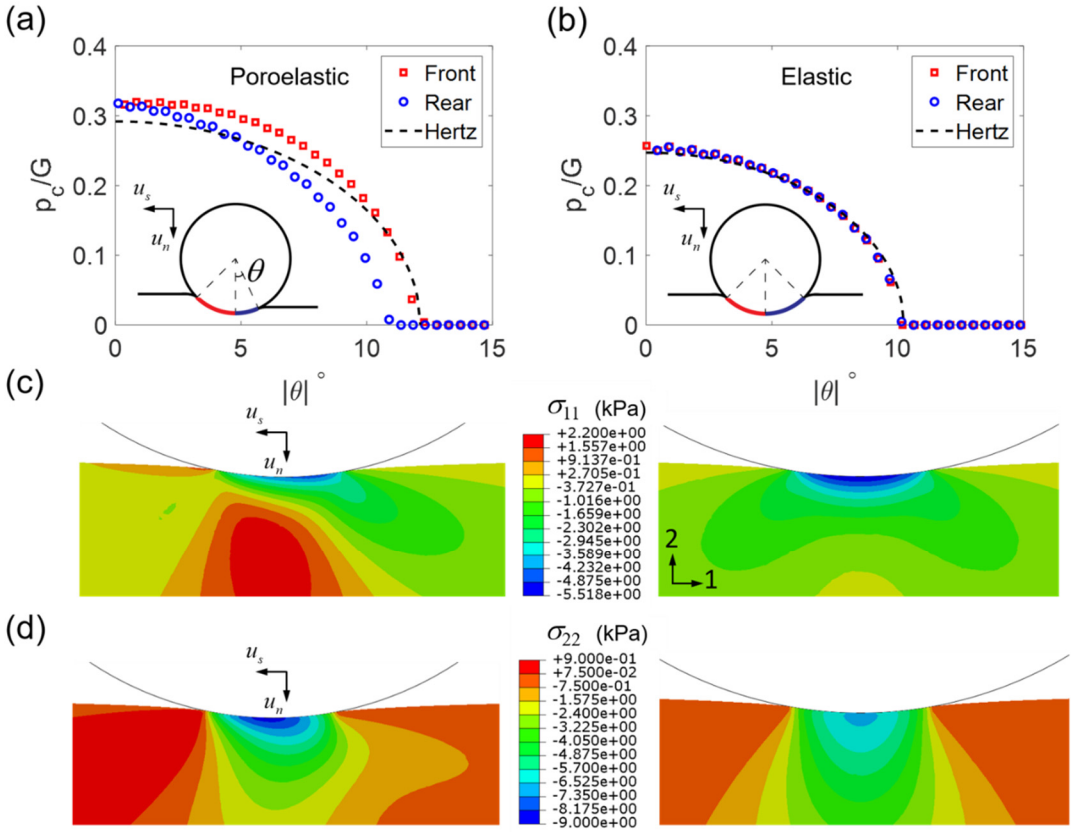

Figure 4 (a-b) Normalized contact pressure p_c/G along the interface for the poroelastic case and the elastic control where u_n= 3mm and V_s = 0.7mm/s. The symbols represent FE results and the dashed line represents the plane strain Hertz solution in eq.(10). (c-d) Contours of the normal stress components (c) σ_{11} and (d) σ_{22} in the substrate for the poroelastic case and the elastic control. The subscripts "1" and "2" denote the horizontal and vertical directions, respectively.

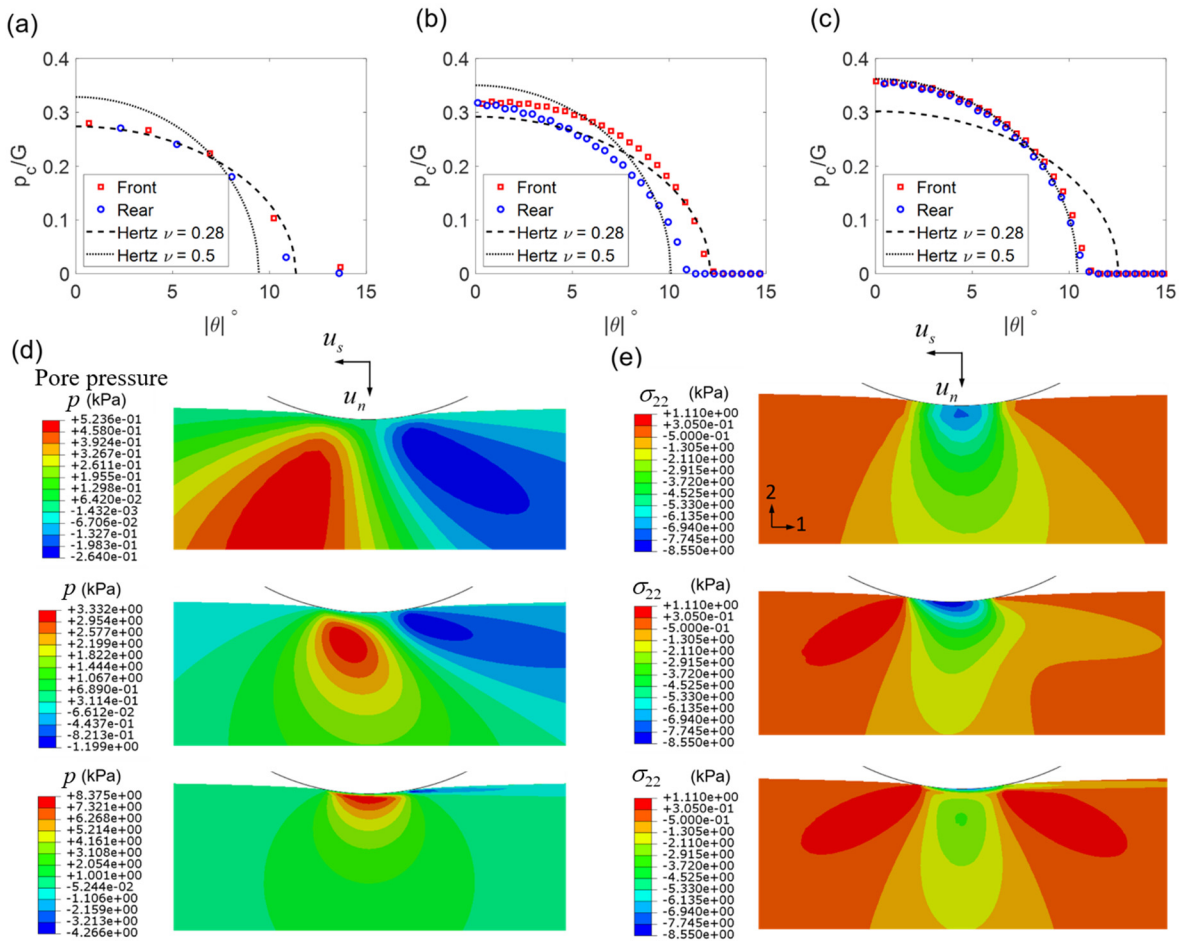

Figure 5 (a-c) Normalized contact pressure p_c/G along the interface for the poroelastic case with u_n= 3mm and three different V_s: (a) 0.05mm/s, (b) 0.7mm/s, and (c) 100mm/s. Also, plotted is the plane strain Hertz solution in eq.(10) with two different Poisson's ratios (0.28 and 0.5) for the drained and undrained states of the poroelastic substrate. (d-e) Contours of (d) pore pressure p and (e) normal stress σ_{22} in the substrate under steady state sliding. In (d-e), the top, middle and bottom rows correspond the cases with V_s = 0.05, 0.7, and 100mm/s, respectively.

The result in Fig.4a leads to the following question: what gives rise to the asymmetric contact pressure in the poroelastic case? To gain insight, we plot the stress fields of σ_{11} and σ_{22} within the substrate in Figs.4c and 4d. Asymmetry in both stress fields is clearly observed for the poroelastic case, in contrast to the symmetric stress fields in the elastic control. Since the pore pressure p is zero at the interface due to the prescribed boundary condition, it does not contribute directly to the contact pressure p_c. Instead, the asymmetric profile of p_c must be related to asymmetric deformation field induced by poroelastic diffusion in the substrate, as manifested by the asymmetric contact width in Fig.4a. As shown in Fig.5, steady state sliding of the indenter can

cause a high pore pressure region in front of the indenter and a low pore pressure region behind it, implying that fluid is driven from the leading edge of the indenter to the trailing edge. This uneven distribution of pore pressure breaks the symmetry of the substrate deformation field, thereby leading to asymmetric contact pressure p_c and hence a net friction force F_s. This mechanism also explains why F_s increases with the normal indentation depth u_n observed in Fig.3b, because a larger u_n gives rise to a wider contact region.

Next, we discuss the rate-dependence of poroelasticity induced friction. Figure 5 shows the results for three cases with u_n = 3 mm and different values of V_s (= 0.05, 0.7 and 100 mm/s) that represent the regimes of low, intermediate and high sliding velocities. Specifically, we first plot the contact pressure distribution for V_s =0.05, 0.7 and 100mm/s in Fig.5a, 5b, and 5c, respectively. Interestingly, the contact pressure is nearly symmetric under both low and high velocities (i.e., 0.05 and 100mm/s), which is consistent with the low friction force in these two regimes as shown in Fig.3a. Figures 5d and 5e show the fields of pore pressure p and normal stress σ_{22} in the substrate for these three cases. At low velocity (V_s =0.05mm/s), the pore pressure field is approximately antisymmetric about the center of the indenter, which consists of a positive p region ahead of the indenter and a negative p region behind it (note that V_s points to the left). However, because the substrate is almost in the drained state due to the low velocity, the magnitude of p is too small to influence σ_{22}. Therefore, σ_{22} is still approximately symmetric about the indenter center. As V_s increases to 0.7mm/s, the magnitude of p is sufficiently large which results in an asymmetric σ_{22} field leading to the asymmetric contact pressure in Fig.5b. At high velocity (V_s =100mm/s), the positive p region dominates and is roughly symmetric about the indenter center, while the negative p region is suppressed. This corresponds to the undrained state of the substrate. Therefore, even though the magnitude of p is high, σ_{22} is again nearly symmetric about the indenter center and so is the contact pressure in Fig.5c. It should be noted that these results were based on the assumption of a zero pore pressure condition on the top surface of the gel substrate, including the contact region. In reality, the impermeable indenter may resist poroelastic diffusion across the contact interface. This condition implies that the flux within the contact region should be finite or even zero (i.e., completely impermeable), while the substrate surface outside the contact region is still subjected to zero pore pressure. However, during steady state sliding the contact region keeps moving, which makes it challenging to prescribe different boundary conditions within and outside the contact region. In Appendix 3, we show that the results in Figs.5a-5c do not change

qualitatively if the zero pore pressure condition on the entire top surface of the gel substrate is replaced by a zero flux condition. Therefore, the assumed zero pore pressure condition at the contact interface does not qualitatively affect our conclusion regarding the asymmetry of contact pressure.

To provide theoretical support for the FE results in Fig.5d, we note that an analytical solution for the plane strain problem of steady state translation of a vertical concentrated force acting on a poroelastic half space is available in the literature (Cheng, 2016). Although our problem involves a circular indenter with a finite radius R, the concentrated force solution can provide a good approximation for material points whose distance to the contact region center is much larger than R. We set up a moving coordinate system centered at the concentrated force with the x-axis pointing horizontally left and y-axis pointing vertically down. The pore pressure field $p(x, y)$ in the substrate is given by Chapter 7.16 of Cheng (2016)

$$p(x,y)=\frac{1}{\pi}\int_0^\infty \mathrm{Im}\left\{i\tilde{p}(y)e^{ilx}\right\}dl\,, \tag{11}$$

$$\tilde{p}(y)=\frac{iF_n(1-\nu)\tilde{V}}{\left[(1-2\nu)\left(\sqrt{1-i\tilde{V}}-1\right)+i(1-\nu)\tilde{V}\right]}\left(e^{-ly}-e^{-ly\sqrt{1-i\tilde{V}}}\right),\ y>0, \tag{12}$$

and

$$\tilde{V}=\frac{V}{Dl}\,, \tag{13}$$

where "Im" in eq.(11) means the imaginary part of a complex number, l is a dummy variable for integration, F_n is the concentrated force (pointing vertically downward), V is the translational velocity of the concentrated force, D is the diffusivity of the poroelastic substrate, and ν is the Poisson's ratio of the drained state. In our problem, the origin of x-y system is located at the center of contact region and the sliding velocity V_s is equivalent to V. Next we consider two limiting cases.

First, in the limit of $V \to \infty$, the first order approximation of eq.(12) is

$$\tilde{p}(y)\approx F_n e^{-ly}, \tag{14}$$

which leads to

$$p(x,y) \approx \frac{F_n}{\pi}\int_0^\infty e^{-ly}\cos(lx)dl = \frac{F_n}{\pi}\frac{y}{x^2+y^2}. \tag{15}$$

This result implies that the pore pressure field is symmetric about the y-axis as $V \to \infty$, which is consistent with the high velocity regime (V_s = 100mm/s) shown in Fig.5d. Moreover, eq.(15) coincides with the hydrostatic pressure field given by the Flamant solution for a vertical downward point force acting on an incompressible elastic half space (Johnson, 1987):

$$-\frac{\sigma_{ss}}{3} = \frac{F_n}{\pi}\frac{y}{x^2+y^2}. \tag{16}$$

Therefore, as the limit of $V \to \infty$, the poroelastic substrate remains in its undrained state and behaves as an incompressible elastic solid.

Second, in the limit of $V \to 0$, the first order approximation of eq.(12) is

$$\tilde{p}(y) \approx 2F_n(1-\nu)e^{-ly}\left(1-e^{\frac{i\tilde{V}ly}{2}}\right), \tag{17}$$

which leads to

$$p(x,y) \approx \frac{F_n(1-\nu)}{\pi}\frac{Vy}{D}\int_0^\infty e^{-ly}\sin(lx')dl = \frac{F_n(1-\nu)V}{\pi D}\frac{xy}{x^2+y^2}. \tag{18}$$

This result has two implications: i) the pore pressure field is antisymmetric about the y-axis as $V \to 0$; ii) the magnitude of pore pressure p scales linearly with V and thus is small, both of which are consistent with the low velocity regime (V_s = 0.05 mm/s) shown in Fig.5d. In this limit, the poroelastic substrate is in the drained state and behaves as a compressible elastic solid.

The drained and undrained limits are further illustrated by plotting the plane strain Hertz solution of contact pressure p_c in Figs.5a-5c. Specifically, we first use the normal force F_n from the FE result to determine the contact width in eq.(9) and then calculate p_c/G using eq.(10). Unlike Figs.4a-4b, here we plot two cases with different Poisson's ratios: ν = 0.28 or 0.5. The former corresponds to the drained limit (compressible) of the gel, and the latter corresponds to the undrained limit (incompressible) of the gel. The contact pressure profiles in the low velocity (see Fig.5a) and high velocity (see Fig.5c) regimes (see Fig.5a) agree well with the drained elastic solution (ν = 0.28) and undrained elastic solution (ν = 0.5), respectively. In the intermediate

velocity regime (see Fig.5b), the contact pressure profile deviates from both elastic solutions. The FE result of p_c near the center of contact region ($|\theta| \sim 0^o$) is bounded between the two elastic solutions, indicating that this is a region of active poroelastic diffusion. Interestingly, p_c approaches the drained elastic solution near the leading edge of the contact region and the undrained elastic solution near the trailing edge of the contact region. This suggests that the substrate material near the leading edge of the contact region is more compliant than that near the trailing edge, which leads to a larger contact width at the leading edge.

Finally, we note that the non-monotonic rate-dependence of friction force and the asymmetric contact region have been experimentally observed by Delavoipière et al. (2018) for a spherical indenter on a thin hydrogel substrate. The friction experiments in Delavoipière et al. (2018) were conducted under fixed normal forces. Therefore, the decrease in friction force at high sliding velocities is accompanied by a reduction in the size of contact area. In contrast, our simulations were performed under fixed normal displacements, where the contact size is approximately the same for different sliding velocities. The rate-dependence of friction force observed in our simulations is mainly caused by the rate-dependent pore pressure field and the asymmetry in contact pressure, as explained above.

3.2 Frictional interface

When a non-zero friction coefficient μ is implemented at the interface, poroelasticity can still contribute to the steady state friction force by inducing an extra net shear force through the mechanism of asymmetric contact pressure. This phenomenon is illustrated in Fig.6 where the friction force F_s versus shear displacement u_s curves are plotted for u_n = 1 mm, V_s = 10 mm/s and three different friction coefficients μ. For cases with non-zero μ, the friction F_s first increases abruptly when u_s is small (see Fig.6b), followed by a more gradual increase of F_s until a plateau is achieved. The first stage (i.e., abrupt increase of F_s) is due to static friction, where the substrate deforms with a fixed contact area and F_s results from frictional shear tractions on the interface. As a result, this stage is absent for $\mu = 0$. The second stage (i.e., gradual increase of F_s) is attributed to poroelastic diffusion associated with indenter sliding, and follows a similar trend for all three cases of μ.

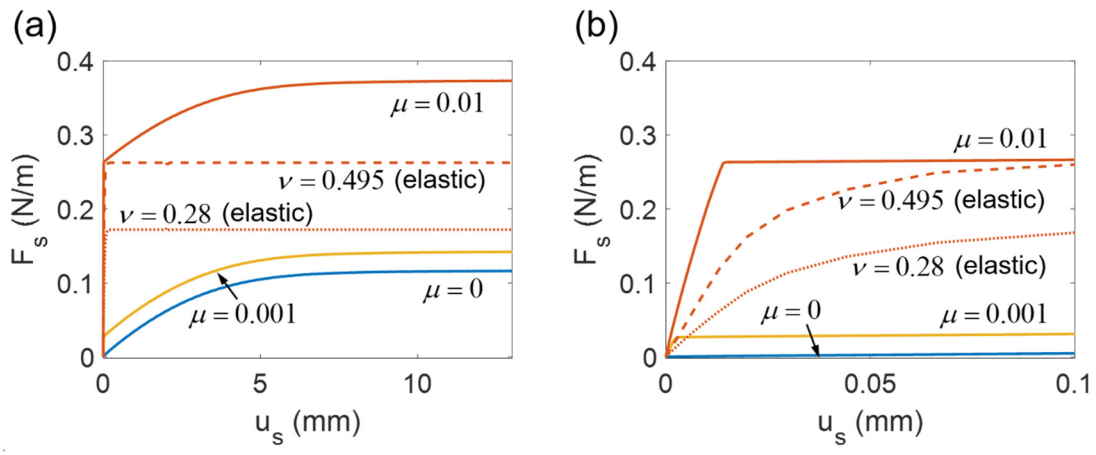

Figure 6 (a) Friction force F_s versus shear displacement u_s for three different interface friction coefficients ($\mu = 0$, 0.001, and 0.01). Also plotted are the results for elastic substrate with the same shear modulus G as the poroelastic substrate and Poisson's ratio $\nu = 0.28$ or 0.495. Note that the normal displacement is fixed at u_n =1mm and the sliding velocity is V_s =10mm/s. (b) A zoom-in view at small u_s to show the abrupt increase of F_s at small u_s.

To highlight the effect of poroelasticity, we take the case of $\mu = 0.01$ as an example and replace the poroelastic substrate by an elastic one with the same G and ν (= 0.28) as the drained limit. Result for the elastic case (ν = 0.28) is shown in Fig.6 as a dotted line. As expected, F_s settles at a constant value once sliding starts. Interestingly, the elastic case (ν = 0.28) exhibits a higher shear compliance than the poroelastic case during the static friction stage (see Fig.6b), and a lower shear force F_s than the poroelastic case at the onset of sliding. We attribute the difference to the fact that the elastic case with ν = 0.28 represents the drained limit and thus is more compliant than the poroelastic substrate. This is evidenced by the dashed line in Fig.6 where we change the Poisson ratio ν of the elastic case to 0.495, i.e., closer to the undrained limit of the poroelastic substrate. The elastic case with ν = 0.495 approaches the poroelastic case during the static friction stage, and the onset of sliding occurs at the same F_s. After the onset of sliding, the friction force in the poroelastic case continues to increase, which corresponds to the transient build-up of asymmetric contact pressure before a steady state is achieved.

4. Relaxation under fixed shear displacement

4.1 Frictionless interface

Poroelastic diffusion in the substrate can also lead to the relaxation of normal force F_n and shear force F_s if the displacements u_n and u_s are fixed. Here we focus on relaxation of the shear force F_s which will be compared with that of the normal force F_n. We start with the frictionless case and apply the loading history in Fig.2c. Specifically, the normal displacement u_n is first increased to 3mm at 10mm/s and then held fixed. After that, the shear displacement u_s is increased to 2mm at a velocity V_s and then held fixed. The relaxation histories of F_s for three cases with different V_s are shown in Fig.7a. Note that the time t is relative to the onset of fixing u_s, which is different for these two cases. The initial value of F_s at the beginning of relaxation ($t = 0$) is different in the three cases due to the rate dependence of F_s under sliding. The long-term limit of F_s is practically zero, which is expected because of the frictionless interface.

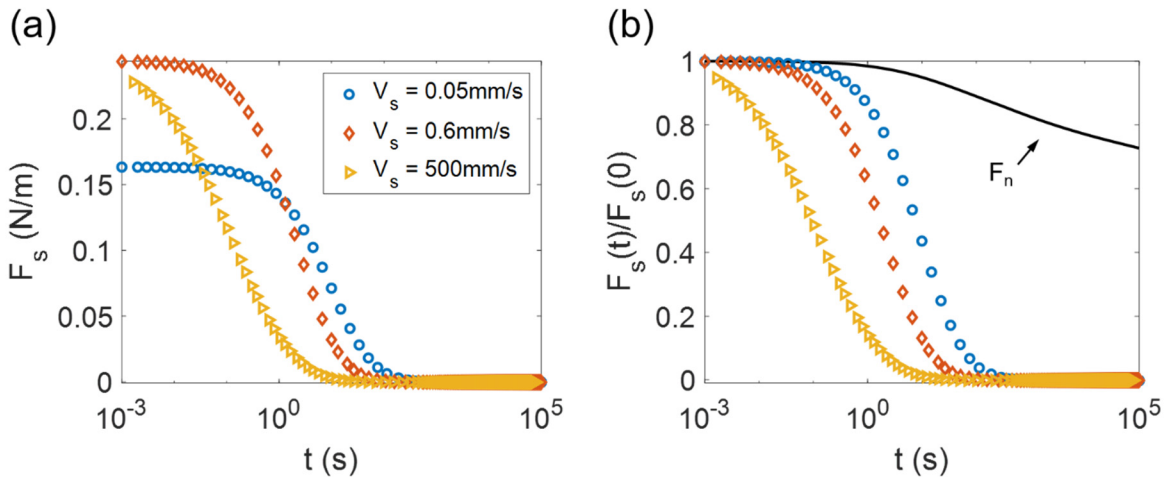

Figure 7 (a) Time history of shear force F_s after u_s is increased to 2mm at V_s = 0.05, 0.6, or 500mm/s and then held fixed. (b) Normalized time history for the normal force F_n (solid line) and shear force F_s (dashed lines).

To facilitate comparison between the relaxation history of F_n and F_s, we plot the force normalized by its initial value at the beginning of relaxation (t =0) in Fig.7b. Again, the time t is not defined in the absolute sense, but rather relative to the onset of fixing u_n (for F_n) or u_s (for F_s). Two important differences between the relaxation of normal and shear forces are observed: i) the shear force F_s relaxes much faster than the normal force F_n; (ii) the shear force F_s relaxes to zero while the normal force F_n relaxes to a plateau value related to the drained state. Both features are consistent with experimental data from literature as shown in Fig.1c. The difference in relaxation time between F_n and F_s is intriguing. In principle, the characteristic relaxation time τ due to

poroelastic diffusion can be estimated by $\tau \sim L^2/D$, where L is the size of the diffusion region involved in relaxation and D is the poroelastic diffusivity (see eq. (6)). The relaxation processes of F_n and F_s should involve the same characteristic length L, i.e., the contact width, and yet exhibit substantially different relaxation times. To understand this behavior, we recall that the shear force F_s on a frictionless substrate relies on asymmetry of the contact region. Poroelastic diffusion not only reduces the contact pressure over time, but also drives interfacial slippage which decreases the extent of contact region asymmetry. While the relaxation of normal force F_n is dominated by the reduction in contact pressure, the relaxation of shear force F_s is governed by the combined effect of contact pressure reduction and interfacial slippage. This mechanism explains why F_s relaxes much faster than F_n. It also implies that the relaxation of F_s is dependent on the loading history, e.g., the sliding velocity V_s before the onset of relaxation can affect the asymmetry of contact region and hence the subsequent time history of relaxation, as shown in Fig.7b.

4.2 Frictional interface

Based on the discussion in Section 4.1, we hypothesize that if interfacial slippage is suppressed, the relaxation history of shear force F_s should approach that of the normal force F_n. To test this hypothesis, we increase the interfacial friction coefficient μ in the FE model and rerun the simulations where the indenter is first moved to a normal displacement u_n (=1, 2, or 3mm) at 10mm/s and then to a shear displacement u_s =2mm at 500mm/s. Figure 8 shows the relaxation histories of F_s for five cases with different μ. Similar behaviors are observed for all three normal displacements u_n. As expected, increasing μ leads to larger F_s over the entire time span of relaxation. More interestingly, the relaxation appears to become slower as μ increases from 0.01 to 2. This is consistent with our hypothesis that larger μ suppresses interfacial slippage and thus slows down the relaxation of F_s.

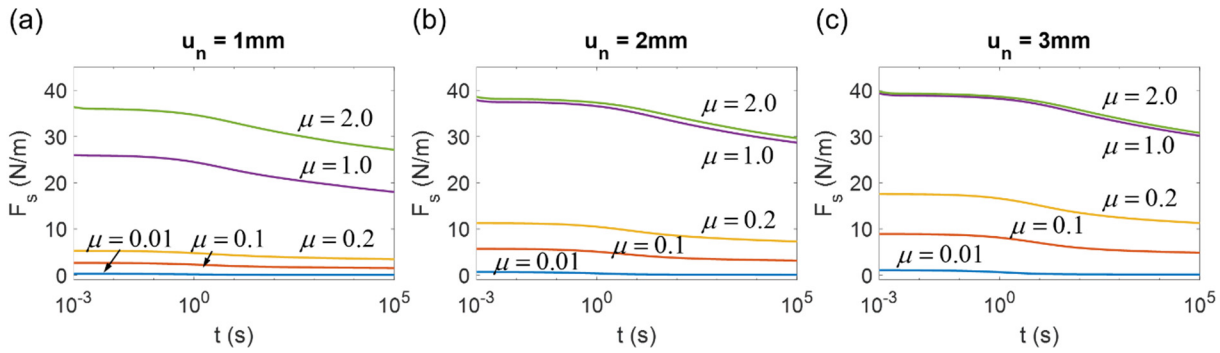

Figure 8 Time history of shear force F_s when u_s is increased to 2mm at V_s =500mm/s and then held fixed. Five cases of interfacial friction coefficient μ (=0.01, 0.1, 0.2, 1, 2) and three fixed normal displacements: (a) u_n=1mm, (b) u_n =2mm, and (c) u_n = 3mm are considered.

We take a closer look at the shear force relaxation by plotting the normalized time history for u_n =3mm in Fig.9a. Also included for comparison is the relaxation time history of the corresponding normal force. As the friction coefficient μ increases from 0.01 to 0.2, the relaxation curve of shear force F_s clearly approaches that of the normal force F_n, both in terms of the relaxation time and the long-term plateau value. However, when μ is as large as 2, we observe a peculiar fast relaxation event occurring before $t \sim 10^{-3}$ s in addition to the main relaxation history. Similar behaviors are observed for μ = 0.8 and 1. Indeed, the normalized relaxation curves for μ = 0.8 and 1 overlaps that for μ = 2 and thus are not shown in Fig.9a. To rule out the possibility of numerical error, we refine the mesh for the case of μ = 2 so that the minimum element size is reduced by 20 times, but still obtain the same result as that in Fig.9a. Next we consider possible physical explanations. Since relaxation is driven by poroelastic diffusion in the substrate, the fast relaxation event observed for μ = 0.8 to 2 indicates that there exists a deformation length scale much smaller than the contact width. One possible mechanism is that the compression at the leading edge due to the shear loading can induce local wrinkling instability. This behavior has been observed in friction experiments between a spherical indenter and a rubber substrate, and serves as the precursor for a phenomenon known as the Schallamach wave (Barquins, 1985). The tendency of local instability within the contact region can provide an additional length scale that is much smaller than contact width. The exact coupling between poroelastic diffusion and local elastic instability is an interesting problem that requires a separate study and is not pursued here.

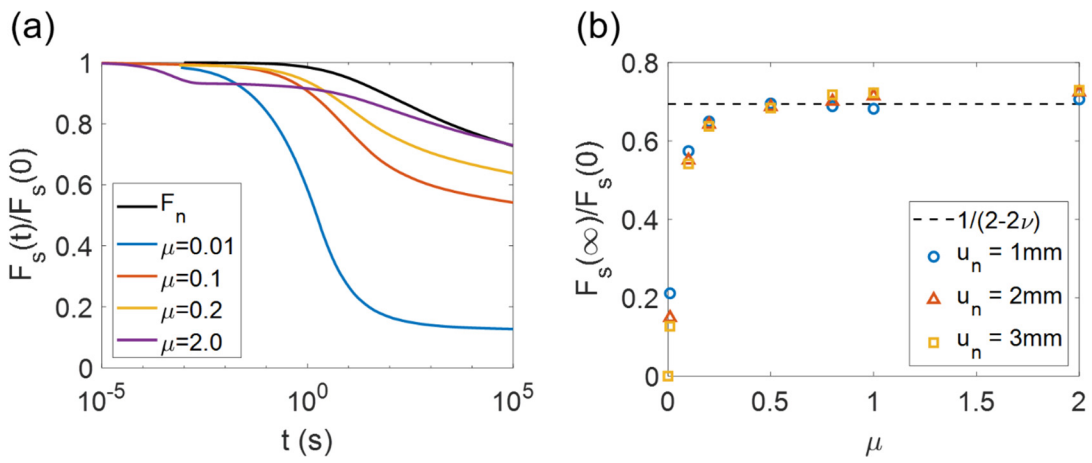

Figure 9 (a) Normalized time history of shear force F_s under u_n =3mm with different interfacial friction coefficients μ and for the corresponding normal force F_n. (b) The long-term plateau value of shear force relaxation $F_s(\infty)/F_s(0)$ versus friction coefficient μ.

Finally, we plot the long-term plateau value of the normalized shear relaxation curve, referred to as $F_s(\infty)/F_s(0)$, but actually evaluated at t =10^5s due to the finite time span of FE results. As shown in Fig.9b, the plateau value increases substantially with μ. Specifically, $F_s(\infty)/F_s(0)$ starts at ~0.2 when μ=0.01 and settles at $1/(2-2\nu)$ when $\mu \geq 0.5$. Note that $1/(2-2\nu)$ is the theoretical plateau value for the normal force relaxation $F_n(\infty)/F_n(0)$, which describes the transition from the undrained state to the drained state of the substrate.

5. Conclusions

We present a computational study on the contact mechanics between a rigid indenter and a poroelastic substrate under plane strain conditions. Our focus is on the resultant shear force on the indenter under two types of loading conditions: i) continuous sliding with a fixed normal displacement and ii) relaxation under fixed normal and shear displacements.

- For continuous sliding, we find that poroelastic diffusion in the substrate can lead to a net shear force even if the contact interface is frictionless. Our FE data reveals that the poroelasticity induced friction originates from the asymmetric pore pressure field in the substrate induced by sliding. This further causes asymmetric contact pressure at the interface and hence the net friction force. The magnitude of such poroelasticity induced friction is sensitive to the sliding

velocity: it diminishes at either low or high sliding velocities, where the substrate behaves as drained or undrained elastic solid, and the peak friction occurs at an intermediate velocity. We find that the rate-dependent pore pressure field within the substrate is responsible for the dependence of friction on sliding velocity. For cases with a non-zero interfacial friction coefficient, poroelasticity can still induce an extra contribution to the steady state friction.

- For relaxation, we find that the poroelasticity induced friction force on a frictionless interface relaxes much faster than the normal force. In addition, the long-term plateau of the relaxation is zero. For cases with a non-zero interfacial friction coefficient, the relaxation curve for friction force approaches that of the normal force as the friction coefficient increases, both in terms of the relaxation time and the long-term plateau.

Although our study is based on idealized plane strain geometry and a linear poroelastic model, the conclusions drawn from the FE results are qualitatively consistent with experimental data in the literature. More importantly, the FE results provide theoretical insights to elucidate the effects of bulk poroelasticity on the friction of gels.

Acknowledgement

The authors would like to thank the National Science Foundation (NSF) for funding this work through grant CMMI-1636203.

Appendix 1 Péclet number

As described in Section 2.1, despite the differences in geometrical dimensions, both Delavoipière et al. (2018) and Reale and Dunn (2017) studied the steady state sliding of a rigid glass sphere on a gel substrate under fixed normal force F_n, and defined Péclet number to describe the competition between poroelastic diffusion and advection induced by sliding. Their definitions of Péclet number are consistent in scaling but are different in values. In Delavoipière et al. (2018), the Péclet number is defined as

$$Pe_1 = \frac{V_s}{a}\frac{a_0^2}{4\frac{k}{\eta}\frac{2(1-\nu)G}{1-2\nu}} = \frac{V_s a}{4D\left(a/a_0\right)^2}\ , \tag{19}$$

where V_s is the sliding velocity, D is the poroelastic diffusivity of the gel, a is the contact radius during steady state sliding and a_0 is the long-term equilibrium contact radius under a fixed normal force F_n. Note that the ratio a/a_0 is smaller than or equal to 1 because of the fixed normal force (rather than fixed normal displacement) during sliding. Indeed, Delavoipière et al. (2018) experimentally found that a/a_0 is roughly 1 when $Pe_1 <\sim 1$, and decreases to ~0.6 for Pe_1 up to 100. In addition, Delavoipière et al. (2018) used a very thin gel substrate, and therefore a_0 was given by a thin film approximation rather than the Hertz theory. In contrast, the Péclet number in Reale and Dunn (2017) is defined as

$$Pe_2 = \frac{2V_s a}{D}. \tag{20}$$

Since $a/a_0 \leq 1$, the difference between eq.(19) and eq.(20) can be as large as eight times.

Delavoipière et al. (2018) found that the peak friction force under steady state sliding occurs at $Pe_1 \sim 1$. Since $a/a_0 \approx 1$ near $Pe_1 \sim 1$, eq.(19) reduces to $Pe_1 \approx V_s a/4D$. Using this approximation and treating a as half of the total contact width, we found that the Péclet number associated with the peak friction in Fig.3a is $Pe_1 = 1\sim1.7$, which is on the same order as the result in Delavoipière et al. (2018). However, due to the large differences in geometry (e.g., plane strain versus spherical indentation; thick substrate versus thin substrate) and loading condition (fixed normal displacement versus fixed normal force) between our model and the experiments in Delavoipière et al. (2018), quantitative comparisons are not pursued here.

Appendix 2 Additional details of the FE simulations

To improve convergence in some cases of FE simulations, we applied the automatic stabilization option in ABAQUS by specifying a constant damping factor (= 0.02), which adds a fictitious viscous force to the global equilibrium equation. Such damping factor does not affect the result. In Fig.10, we plot the result of shear force F_s versus shear displacement u_s under continuous sliding either using a damping factor of 0.02 or with no damping factor. The results are nearly identical.

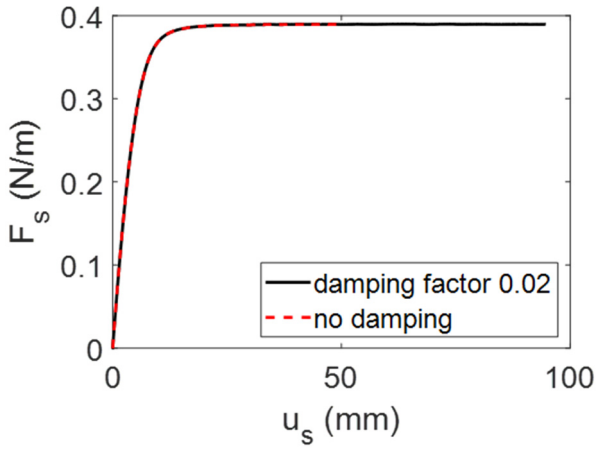

Figure 10 Effect of damping factor on the FE results. Shear force F_s versus shear displacement u_s under continuous sliding with a fixed normal displacement u_n =2mm and sliding velocity V_s = 5mm/s.

Even though we set the lateral width of the gel substrate w to be much larger than indenter radius R (i.e., $w = 100R$), our FE results still exhibit a minor dependence on w. This is attributed to the well-known unbounded far field displacements in the Flamant solution and consequently the plane strain contact mechanics solution with an elastic half space (Johnson, 1987). For example, by increasing the w to be $200R$, the shear force F_s increases slightly, as shown in Fig.11a. However, the quantitative trend of the function F_s versus V_s is independent of w.

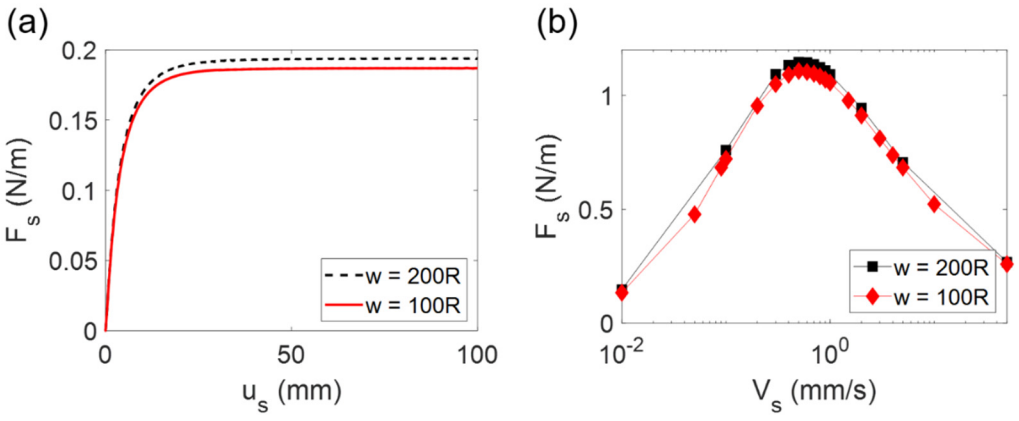

Figure 11 Effect of the substrate width w on the FE results. (a) Shear force F_s versus shear displacement u_s under continuous sliding with a fixed normal displacement u_n =1mm and sliding velocity V_s = 0.6mm/s. (b) Dependence of the steady state friction force F_s on the sliding velocity V_s for the normal displacement of u_n =3mm.

Appendix 3 Effect of poroelastic boundary condition

To illustrate the effect of poroelastic boundary condition, we replaced the zero pore pressure condition at the entire top surface of the gel substrate by a zero flux condition, and reran the simulations of steady state sliding shown in Figs.5a-5c. Results based on the zero pore pressure condition or the zero flux condition are compared in Fig.12. One can see that the zero flux condition leads to a slight increase in contact pressure, but does not qualitatively change the results.

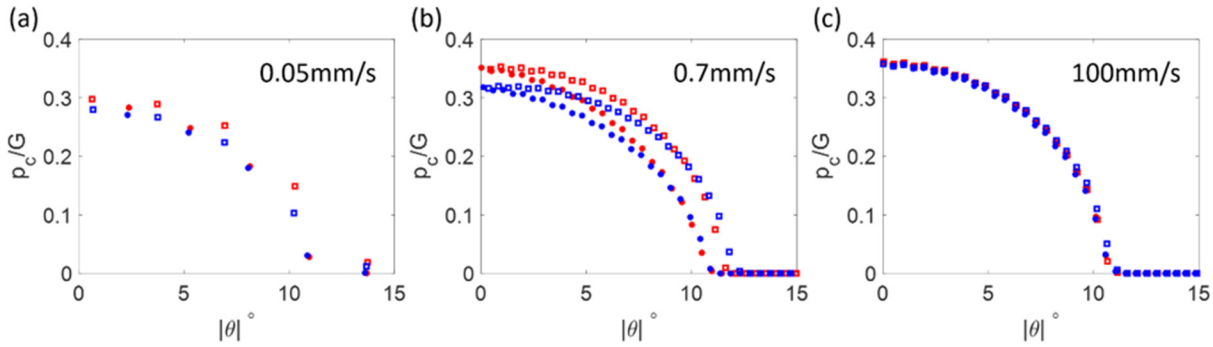

Figure 12 Normalized contact pressure p_c/G along the interface for the poroelastic case with u_n= 3mm and three different V_s: (a) 0.05mm/s, (b) 0.7mm/s, and (c) 100mm/s. The open square symbols represent points near the leading edge, while the closed circular symbols represent points near the trailing edge. The blue symbols are obtained using a zero pore pressure condition on the top surface of gel substrate, while the red symbols represent the results using a zero flux condition.

References

Ateshian, G.A., 2009. The role of interstitial fluid pressurization in articular cartilage lubrication. J. Biomech. 42, 1163–1176. https://doi.org/10.1016/j.jbiomech.2009.04.040

Barquins, M., 1985. Sliding friction of rubber and Schallamach waves - A review. Mater. Sci. Eng. https://doi.org/10.1016/0025-5416(85)90295-2

Barthel, E., Frétigny, C., 2009. Adhesive contact of elastomers: effective adhesion energy and creep function. J. Phys. D. Appl. Phys. 42, 195302. https://doi.org/10.1088/0022-3727/42/19/195302

Bhushan, B., 2003. Adhesion and stiction: Mechanisms, measurement techniques, and methods for reduction. J. Vac. Sci. Technol. B Microelectron. Nanom. Struct. 21, 2262–2296. https://doi.org/10.1116/1.1627336

Cheng, A.H.-D., 2016. Poroelasticity. Springer, Berlin, Heidelberg. https://doi.org/https://doi.org/10.1007/978-3-319-25202-5

Delavoipière, J., Tran, Y., Verneuil, E., Heurtefeu, B., Hui, C.Y., Chateauminois, A., 2018. Friction of Poroelastic Contacts with Thin Hydrogel Films. Langmuir 34, 9617–9626. https://doi.org/10.1021/acs.langmuir.8b01466

Dunn, A.C., Urueña, J.M., Huo, Y., Perry, S.S., Angelini, T.E., Sawyer, W.G., 2013. Lubricity of surface hydrogel layers. Tribol. Lett. 49, 371–378. https://doi.org/10.1007/s11249-012-0076-8

Gong, J., Higa, M., Iwasaki, Y., Katsuyama, Y., Osada, Y., 1997. Friction of Gels. J. Phys. Chem. B 101, 5487–5489. https://doi.org/10.1021/JP9713118

Gong, J., Iwasaki, Y., Osada, Y., Kurihara, K., Hamai, Y., 2002. Friction of Gels. 3. Friction on Solid Surfaces. J. Phys. Chem. B 103, 6001–6006. https://doi.org/10.1021/jp9902553

Gong, J., Osada, Y., 1998. Gel friction: A model based on surface repulsion and adsorption. J. Chem. Phys. 109, 8062–8068. https://doi.org/10.1063/1.477453

Gong, J.P., 2006. Friction and lubrication of hydrogels—its richness and complexity. Soft Matter 2, 544–552. https://doi.org/10.1039/B603209P

Greene, G.W., Banquy, X., Lee, D.W., Lowrey, D.D., Yu, J., Israelachvili, J.N., 2011. Adaptive mechanically controlled lubrication mechanism found in articular joints. Proc. Natl. Acad. Sci. 108, 5255–5259. https://doi.org/10.1073/pnas.1101002108

Greene, G.W., Zappone, B., Zhao, B., Söderman, O., Topgaard, D., Rata, G., Israelachvili, J.N., 2008. Changes in pore morphology and fluid transport in compressed articular cartilage and the implications for joint lubrication. Biomaterials 29, 4455–4462. https://doi.org/10.1016/j.biomaterials.2008.07.046

Hu, Y., Chan, E.P., Vlassak, J.J., Suo, Z., 2011. Poroelastic relaxation indentation of thin layers of gels. J. Appl. Phys. 110, 086103. https://doi.org/10.1063/1.3647758

Hu, Y., Zhao, X., Vlassak, J.J., Suo, Z., 2010. Using indentation to characterize the poroelasticity of gels. Appl. Phys. Lett. 96, 121904. https://doi.org/10.1063/1.3370354

Hui, C.-Y., Lin, Y.Y., Chuang, F.-C., Shull, K.R., Lin, W.-C., 2006. A contact mechanics method for characterizing the elastic properties and permeability of gels. J. Polym. Sci. Part B Polym. Phys. 44, 359–370. https://doi.org/10.1002/polb.20613

Jin, Z.M., Dowson, D., Fisher, J., 1992. The Effect of Porosity of Articular Cartilage on the Lubrication of a Normal Human Hip Joint. Proc. Inst. Mech. Eng. Part H J. Eng. Med. 206, 117–124. https://doi.org/10.1243/PIME_PROC_1992_206_279_02

Johannes, K., Calahan, K.N., Qi, Y., Long, R., Rentschler, M.E., 2019. Three-Dimensional Microscale Imaging and Measurement of Soft Material Contact Interfaces Under Quasi-Static Normal Indentation and Shear. Langmuir 35, 10725–10733. https://doi.org/10.1021/acs.langmuir.9b00830

Johnson, K.L., 1987. Contact Mechanics. Cambridge University Press.

Kagata, G., Gong, J.P., Osada, Y., 2002. Friction of gels. 6. Effects of sliding velocity and viscoelastic responses of the network. J. Phys. Chem. B 106, 4596–4601. https://doi.org/10.1021/jp012380w

Krishnan, R., Kopacz, M., Ateshian, G.A., 2004. Experimental verification of the role of interstitial fluid pressurization in cartilage lubrication. J. Orthop. Res. 22, 565–570.

https://doi.org/10.1016/j.orthres.2003.07.002

Kurokawa, T., Tominaga, T., Katsuyama, Y., Kuwabara, R., Furukawa, H., Osada, Y., Gong, J.P., 2005. Elastic-hydrodynamic transition of gel friction. Langmuir 21, 8643–8648. https://doi.org/10.1021/la050635h

McCutchen, C.W., 1962. The frictional properties of animal joints. Wear 5, 1–17. https://doi.org/10.1016/0043-1648(62)90176-X

Moore, A.C., Burris, D.L., 2014. An analytical model to predict interstitial lubrication of cartilage in migrating contact areas. J. Biomech. 47, 148–153. https://doi.org/10.1016/j.jbiomech.2013.09.020

Persson, B.N.J., Scaraggi, M., 2018. Some Comments on Hydrogel and Cartilage Contact Mechanics and Friction. Tribol. Lett. 66, 23. https://doi.org/10.1007/s11249-017-0973-y

Pitenis, A.A., Urueña, J.M., McGhee, E.O., Hart, S.M., Reale, E.R., Kim, J., Schulze, K.D., Marshall, S.L., Bennett, A.I., Niemi, S.R., Angelini, T.E., Sawyer, W.G., Dunn, A.C., 2017. Challenges and opportunities in soft tribology. Tribol. - Mater. Surfaces Interfaces 11, 180–186. https://doi.org/10.1080/17515831.2017.1400779

Pult, H., Tosatti, S.G.P., Spencer, N.D., Asfour, J.M., Ebenhoch, M., Murphy, P.J., 2015. Spontaneous Blinking from a Tribological Viewpoint. Ocul. Surf. 13, 236–249. https://doi.org/10.1016/j.jtos.2014.12.004

Reale, E.R., Dunn, A.C., 2017. Poroelasticity-driven lubrication in hydrogel interfaces. Soft Matter 13, 428–435. https://doi.org/10.1039/c6sm02111e

Rennie, A.C., Dickrell, P.L., Sawyer, W.G., 2005. Friction coefficient of soft contact lenses: measurements and modeling. Tribol. Lett. 18, 499–504. https://doi.org/10.1007/s11249-005-3610-0

Schallamach, A., 1963. A theory of dynamic rubber friction. Wear 6, 375–382. https://doi.org/10.1016/0043-1648(63)90206-0

Shoaib, T., Espinosa-Marzal, R.M., 2018. Insight into the Viscous and Adhesive Contributions to Hydrogel Friction. Tribol. Lett. 66, 96. https://doi.org/10.1007/s11249-018-1045-7

Shoaib, T., Heintz, J., Lopez-Berganza, J.A., Muro-Barrios, R., Egner, S.A., Espinosa-Marzal, R.M., 2018. Stick-Slip Friction Reveals Hydrogel Lubrication Mechanisms. Langmuir 34, 756–765. https://doi.org/10.1021/acs.langmuir.7b02834

Sliker, L.J., Kern, M.D., Schoen, J.A., Rentschler, M.E., 2012. Surgical evaluation of a novel tethered robotic capsule endoscope using micro-patterned treads. Surg. Endosc. 26, 2862–2869. https://doi.org/10.1007/s00464-012-2271-y

Sliker, L.J., Wang, X., Schoen, J.A., Rentschler, M.E., 2010. Micropatterned Treads for In Vivo Robotic Mobility. J. Med. Device. 4, 041006. https://doi.org/10.1115/1.4002761

Smyth, P.A., Green, I., 2017. Analysis of Coupled Poroviscoelasticity and Hydrodynamic Lubrication. Tribol. Lett. 65. https://doi.org/10.1007/s11249-016-0787-3

Sterner, O., Karageorgaki, C., Zürcher, M., Zürcher, S., Scales, C.W., Fadli, Z., Spencer, N.D.,

Tosatti, S.G.P., 2017. Reducing Friction in the Eye: A Comparative Study of Lubrication by Surface-Anchored Synthetic and Natural Ocular Mucin Analogues. ACS Appl. Mater. Interfaces 9, 20150–20160. https://doi.org/10.1021/acsami.6b16425

Yamamoto, T., Kurokawa, T., Ahmed, J., Kamita, G., Yashima, S., Furukawa, Y., Ota, Y., Furukawa, H., Gong, J.P., 2014. In situ observation of a hydrogel-glass interface during sliding friction. Soft Matter 10, 5589–5596. https://doi.org/10.1039/c4sm00338a

Yashima, S., Takase, N., Kurokawa, T., Gong, J.P., 2014. Friction of hydrogels with controlled surface roughness on solid flat substrates. Soft Matter 10, 3192–3199. https://doi.org/10.1039/c3sm52883a